

# Reduced-MHD Simulations of Toroidally and Poloidally Localized ELMs

M. Hölzl<sup>1</sup>, S. Günter<sup>1</sup>, R.P. Wenninger<sup>2</sup>, W.-C. Müller<sup>1</sup>,  
G.T.A. Huysmans<sup>3</sup>, K. Lackner<sup>1</sup>, I. Krebs<sup>1</sup>, and the ASDEX Upgrade  
Team<sup>1</sup>

<sup>1</sup>*Max-Planck-Institut für Plasmaphysik, EURATOM Association, Boltzmannstraße 2, 85748 Garching, Germany*

<sup>2</sup>*Universitätssternwarte der Ludwig-Maximilians-Universität, 81679 München, Germany*

<sup>3</sup>*ITER Organisation, Route de Vinon sur Verdon, St-Paul-lez-Durance, France*

## Abstract

We use the non-linear reduced-MHD code JOEKE to study ELMs in the geometry of the ASDEX Upgrade tokamak. Toroidal mode numbers, poloidal filament sizes, and radial propagation speeds of filaments into the scrape-off layer are in good agreement with observations for type-I ELMs in ASDEX Upgrade. The observed instabilities exhibit a toroidal and poloidal localization of perturbations which is compatible with the “solitary magnetic perturbations” recently discovered in ASDEX Upgrade [R.Wenninger et.al., Solitary Magnetic Perturbations at the ELM Onset, Nucl.Fusion, accepted, preprint at <http://arxiv.org/abs/1202.3603>]. This localization can only be described in numerical simulations with high toroidal resolution.

## 19 **1. Introduction**

20 Edge localized modes (ELMs) accompany the high-confinement mode (H-mode) in tokamak  
21 fusion plasmas. As they could cause a potentially destructive heat-load on divertor plates and  
22 wall structures in large fusion devices [1, 2], detailed understanding of these instabilities and  
23 of mitigation-techniques is important for a successful operation of ITER. Non-linear MHD-  
24 simulations with the JOEKE code [3–9], which is also used for the present article, and other  
25 codes like BOUT++ [10], NIMROD [11], or M3D [12] can make an important contribution  
26 after successful benchmarks with measurements in existing tokamaks.

27 In the present article, a comparison between simulations with the non-linear finite-element code  
28 JOEKE [13] and observations in the ASDEX Upgrade tokamak [14] is started. We concentrate  
29 on the early phase of ELMs. JOEKE solves the reduced MHD equations in realistic X-point  
30 geometries as described in Section 2. ASDEX Upgrade is equipped with a unique set of edge di-  
31 agnostics that allows to investigate ELM crashes with high spatial and temporal resolutions [15].  
32 This provides excellent possibilities for theory-experiment comparisons. Emphasis is put on  
33 simulations with high toroidal resolution (many toroidal modes at toroidal periodicity 1) to treat  
34 the coupling between various toroidal modes properly. This way, aspects can be identified that  
35 are described well already at low toroidal resolution (few toroidal modes at a high toroidal peri-  
36 odicity) while others are influenced significantly by the non-linear toroidal mode-coupling.

37 The article is structured as follows. Section 2 describes the non-linear MHD-code JOEKE.  
38 Physical parameters and technical details of the numerical simulations are given in Section 3.  
39 Our observations and findings made in the simulated instabilities are presented in Section 4.  
40 Subsequently, Section 5 describes how these results compare to experimental measurements.  
41 Finally, Section 6 summarizes and gives a brief outlook.

## 42 **2. JOEKE Code**

43 The simulations are carried out with the single-fluid reduced-MHD model of the JOEKE code.  
44 Section 2.1 describes the equations solved in this model. For more details on the derivation, refer  
45 to Reference [16] and Appendix A. Spatial and temporal discretizations are briefly addressed in  
46 Section 2.2.

Table 1: The normalization of quantities in JOREK is listed, it corresponds to choosing scale factors  $B_0 = 1$  T and  $R_0 = 1$  m. Variable names with subscript ‘‘SI’’ denote quantities in SI units, while variables without this subscript are the ones used in JOREK. In the presented simulations,  $n_0 = 6 \cdot 10^{19} \text{ m}^{-3}$  and  $\rho_0 = 2 \cdot 10^{-7} \text{ kg m}^{-3}$ . The magnetic constant is denoted  $\mu_0$  and the Boltzmann constant  $k_B$ .

$R_{\text{SI}}$ [m]	$= R$	Major radius
$Z_{\text{SI}}$ [m]	$= Z$	Vertical coordinate
$\mathbf{B}_{\text{SI}}$ [T]	$= \mathbf{B}$	Magnetic field vector; see Eq. (9)
$\Psi_{\text{SI}}$ [T m <sup>2</sup> ]	$= \Psi$	Poloidal magnetic flux
$j_{\phi,\text{SI}}$ [A m <sup>-2</sup> ]	$= -j/(R \mu_0)$	Toroidal current density; $j_{\phi,\text{SI}} = \mathbf{j}_{\text{SI}} \cdot \hat{\mathbf{e}}_{\phi}$
$n_{\text{SI}}$ [m <sup>-3</sup> ]	$= \rho n_0$	Particle density
$\rho_{\text{SI}}$ [kg m <sup>-3</sup> ]	$= \rho \rho_0$	Mass density = ion mass $\times$ particle density
$T_{\text{SI}}$ [K]	$= T/(k_B \mu_0 n_0)$	Temperature = electron + ion temperature
$p_{\text{SI}}$ [N m <sup>-2</sup> ]	$= \rho T/\mu_0$	Plasma pressure
$\mathbf{v}_{\text{SI}}$ [m s <sup>-1</sup> ]	$= \mathbf{v}/\sqrt{\mu_0 \rho_0}$	Velocity vector; see Eq. (8)
$v_{\parallel,\text{SI}}$ [m s <sup>-1</sup> ]	$= v_{\parallel} \cdot B_{\text{SI}}/\sqrt{\mu_0 \rho_0}$	Parallel velocity component, where $B_{\text{SI}} =  \mathbf{B}_{\text{SI}} $
$u_{\text{SI}}$ [m s <sup>-1</sup> ]	$= u/\sqrt{\mu_0 \rho_0}$	Velocity stream function
$\omega_{\phi,\text{SI}}$ [m <sup>-1</sup> s <sup>-1</sup> ]	$= \omega/\sqrt{\mu_0 \rho_0}$	Toroidal vorticity; see Eq. (2)
$t_{\text{SI}}$ [s]	$= t \cdot \sqrt{\mu_0 \rho_0}$	Time
$\gamma_{\text{SI}}$ [s <sup>-1</sup> ]	$= \gamma/\sqrt{\mu_0 \rho_0}$	Growth rate; $\gamma_{\text{SI}} = \ln[E_{\text{SI}}(t_2)/E_{\text{SI}}(t_1)]/[2\Delta t_{\text{SI}}]$ ; Energy $E_{\text{SI}}$ [J]
$\eta_{\text{SI}}$ [ $\Omega$ m]	$= \eta \cdot \sqrt{\mu_0/\rho_0}$	Resistivity
$\nu_{\text{SI}}$ [kg m <sup>-1</sup> s <sup>-1</sup> ]	$= \nu \cdot \sqrt{\rho_0/\mu_0}$	Dynamic viscosity
$D_{\text{SI}}$ [m <sup>2</sup> s <sup>-1</sup> ]	$= D/\sqrt{\mu_0 \rho_0}$	Particle diffusivity ( $\parallel$ or $\perp$ )
$K_{\text{SI}}$ [m <sup>-1</sup> s <sup>-1</sup> ]	$= K \cdot n_0/\sqrt{\mu_0 \rho_0}$	Heat diffusivity ( $\parallel$ or $\perp$ ), where $\chi_{\text{SI}}$ [m <sup>2</sup> s <sup>-1</sup> ] = $K_{\text{SI}}/n_{\text{SI}}$
$S_{T,\text{SI}}$ [W m <sup>-3</sup> ]	$= S_T/\sqrt{\mu_0^3 \rho_0}$	Heat source
$S_{\rho,\text{SI}}$ [kg s <sup>-1</sup> m <sup>-3</sup> ]	$= S_{\rho} \cdot \sqrt{\rho_0/\mu_0}$	Particle source

47 **2.1. Reduced-MHD Equations**

48 Seven physical variables are treated: poloidal flux  $\Psi$ , stream function  $u$ , toroidal current density  
 49  $j$ , toroidal vorticity  $\omega$ , density  $\rho$ , temperature  $T$ , and velocity  $v_{||}$  along magnetic field lines. The  
 50 normalization of the relevant quantities is listed in Table 1.

51 Variables  $j$  and  $\omega$  are connected to  $\Psi$  and  $u$  by the definition equations

$$j = \Delta^* \Psi = R^2 \nabla_{pol} \cdot (R^{-2} \nabla_{pol} \Psi) = R \frac{d}{dR} \left( \frac{1}{R} \frac{d\Psi}{dR} \right) + \frac{d^2 \Psi}{dZ^2}, \quad (1)$$

$$\omega = \nabla_{pol}^2 u = \frac{1}{R} \frac{d}{dR} \left( R \frac{du}{dR} \right) + \frac{d^2 u}{dZ^2}, \quad (2)$$

52 where  $\nabla_{pol}$  denotes the del-operator in the poloidal plane,  $R$  the major radius, and  $Z$  the vertical  
 53 coordinate. The time-evolution of the remaining five free variables is described by the following  
 54 set of equations (called physics-model “302” in JOREK):

$$\frac{\partial \Psi}{\partial t} = \eta j - R[u, \Psi] - F_0 \frac{\partial u}{\partial \phi}, \quad (3)$$

$$\frac{\partial \rho}{\partial t} = -\nabla \cdot (\rho \mathbf{v}) + \nabla \cdot (D_{\perp} \nabla_{\perp} \rho) + S_{\rho}, \quad (4)$$

$$\rho \frac{\partial T}{\partial t} = -\rho \mathbf{v} \cdot \nabla T - (\kappa - 1) p \nabla \cdot \mathbf{v} + \nabla \cdot (K_{\perp} \nabla_{\perp} T + K_{||} \nabla_{||} T) + S_T, \quad (5)$$

$$\hat{\mathbf{e}}_{\phi} \cdot \nabla \times \left\{ \rho \frac{\partial \mathbf{v}}{\partial t} = -\rho (\mathbf{v} \cdot \nabla) \mathbf{v} - \nabla p + \mathbf{j} \times \mathbf{B} + \nu \Delta \mathbf{v} \right\}, \quad (6)$$

$$\mathbf{B} \cdot \left\{ \rho \frac{\partial \mathbf{v}}{\partial t} = -\rho (\mathbf{v} \cdot \nabla) \mathbf{v} - \nabla p + \mathbf{j} \times \mathbf{B} + \nu \Delta \mathbf{v} \right\}. \quad (7)$$

55 In every time-step, Equations (1–7) are solved simultaneously in weak form as a large sparse  
 56 implicit system of equations. The velocity vector is defined as

$$\mathbf{v} = -R \nabla u \times \hat{\mathbf{e}}_{\phi} + v_{||} \mathbf{B}, \quad (8)$$

Table 2: The toroidal mode numbers resolved in simulations with different periodicities are listed.

Periodicity	Resolved $n$ -modes
8	0, 8, 16
4	0, 4, 8, 12, 16
2	0, 2, 4, ..., 12, 14, 16
1	0, 1, 2, ..., 14, 15, 16

57 the magnetic field vector as

$$\mathbf{B} = (F_0 \hat{\mathbf{e}}_\phi + \nabla\Psi \times \hat{\mathbf{e}}_\phi)/R, \quad (9)$$

58 the pressure is  $p = \rho T$ , and  $\kappa = 5/3$  denotes the ratio of specific heats. Here,  $\hat{\mathbf{e}}_\phi$  denotes the  
59 normalized toroidal basis vector. The toroidal magnetic field  $B_\phi = F_0/R$  is fixed and cannot  
60 change with time. The poloidal velocity, i.e., the velocity vector in the poloidal plane, is denoted  
61  $\mathbf{v}_{\text{pol}}$ . The parallel gradient is given by  $\nabla_{\parallel} = \mathbf{b}(\mathbf{b} \cdot \nabla)$ , where  $\mathbf{b} = \mathbf{B}/|\mathbf{B}|$ , and the perpendicular  
62 gradient by  $\nabla_{\perp} = \nabla - \nabla_{\parallel}$ . The Poisson bracket  $[u, \Psi]$  is defined as  $\frac{\partial u}{\partial R} \frac{\partial \Psi}{\partial Z} - \frac{\partial u}{\partial Z} \frac{\partial \Psi}{\partial R}$ . Note, that the  
63 poloidal components of the velocity in this set of equations are determined only by the  $\mathbf{E} \times \mathbf{B}$ -  
64 drift term. As a result,  $u$  acts as a velocity stream function and (except for a factor  $F_0$ ) also as  
65 electric potential.

66 Ideal-wall boundary conditions are implemented where the boundary of the computational do-  
67 main is parallel to the magnetic flux surfaces. At the divertor targets, where the flux surfaces  
68 intersect the computational boundary, modified Bohm boundary conditions apply [4, 17].

## 69 2.2. Discretization

70 The poloidal plane is discretized by 2D Bezier finite elements with four degrees of freedom per  
71 grid node and physical variable [13], while a Fourier decomposition is applied toroidally. The  
72 number of toroidal modes resolved in the simulations and the assumed toroidal periodicity of the  
73 system can be chosen separately. A periodicity equal to one means that the solution is computed  
74 for the whole torus. For larger periodicities, only a toroidal section of the torus is resolved. The  
75 modes included in the presented simulations are listed in Table 2.

76 The temporal discretization is performed by a fully implicit second-order linearized Crank-  
77 Nicholson scheme [18]. In the resulting large sparse system, all physical equations and all

Table 3: Core values for plasma resistivity and viscosity are listed for the simulations denoted `eta5` and `eta6`. Both quantities are modeled with a  $T^{-3/2}$  dependence and are chosen significantly larger than in experiments due to computational restrictions. In ASDEX Upgrade, the core resistivity is typically about  $10^{-8} \Omega \text{ m}$ .

Run	$\eta_{\text{SI}} [\Omega \text{ m}]$	$\nu_{\text{SI}} [\text{m}^2/\text{s}]$
<code>eta5</code>	$5 \times 10^{-5}$	$7.5 \times 10^{-5}$
<code>eta6</code>	$5 \times 10^{-6}$	$7.5 \times 10^{-6}$

toroidal harmonics are coupled. It is solved by an iterative GMRES-method, where a physics-based preconditioning is applied at the beginning of each GMRES solver step. In the preconditioning, the coupling between the sub-matrices corresponding to individual toroidal harmonics is neglected which allows to solve each sub-system separately. This is performed using the direct solver PaStiX [19].

### 3. Simulations

Simulations of edge-localized modes are one of the most challenging tasks in fusion MHD numerics. The problem must be treated in realistic X-point geometry as the mode-affected region extends from inside the H-mode pedestal into the scrape-off layer, the vacuum region, and to the divertor legs. High spatial resolutions in all dimensions are required due to the small scales of the structures and the large radial gradients of equilibrium quantities at the pedestal. Thus, as a consequence of limited computational resources, not all aspects of an experiment can be described realistically in simulations so far. For instance, simulations with high resolution in radial and poloidal directions, i.e., with a large number of 2D Bezier finite-elements in the case of JOREK, render important investigations at more realistic plasma resistivities possible (e.g., Ref. [8]), but only at a very limited number of toroidal Fourier harmonics.

For this work, a different choice was made: The focus is put on high toroidal resolution. This is done to investigate the influence of toroidal mode-coupling onto the non-linear evolution of an ELM. The mode numbers resolved in the simulations are listed in Table 2. All runs resolve the  $n = 0, \dots, 16$  range but with different periodicities. The relatively high number of toroidal modes involved limits the possible radial and poloidal resolutions: Most simulations are carried out with about 5500 Bezier elements. The corresponding finite-element grid is shown in Figure 1. Only for the simulations with lower plasma resistivity (denoted “`eta6`” runs, see next paragraph for details), the number of Bezier elements is increased by a factor of two. Grid accumulation is used to increase the resolution radially around the separatrix and poloidally around the X-point.

Due to the comparably low poloidal resolution, only plasma resistivities significantly larger than in the experiment can be resolved. The respective simulation parameters are listed in Table 3.

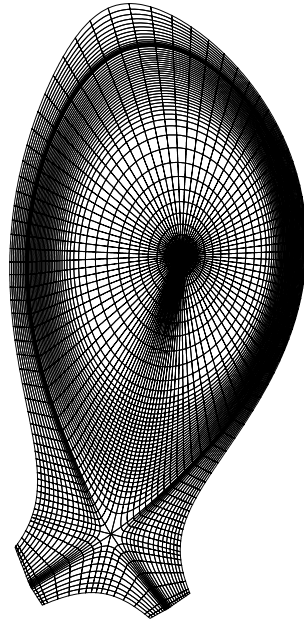


Figure 1: The flux-surface aligned X-point grid with 5500 Bezier finite-elements is shown. The number of grid points are: 96 poloidal points, 40 radial points inside the separatrix, 15 radial points outside the separatrix, 9 “radial” points in the private flux region, and 9 grid points along the divertor legs. For the `eta6` simulations, these numbers are all increased by a factor of  $\sqrt{2}$ , leading to about 11000 Bezier elements.

105 The limited poloidal resolution also reduces the growth rate of modes with high mode numbers  
 106 artificially. Thus when increasing the poloidal resolution, the most unstable mode number would  
 107 shift towards larger  $n$ . On the other hand, diamagnetic stabilization is not taken into account in  
 108 the simulations. Including this effect would have a stabilizing effect onto high poloidal mode  
 109 numbers. The electron diamagnetic frequency for  $n = 10$  is about  $10^5 \text{ s}^{-1}$  (calculated at a nor-  
 110 malized poloidal flux of  $\Psi_N = 0.9$ ). This is comparable to the fastest linear growth rates in the  
 111 simulations (see Section 4). Thus, the most unstable mode numbers would probably be similar  
 112 in simulations with higher poloidal resolution and diamagnetic stabilization taken into account.

113 All simulations are based on typical ASDEX Upgrade discharge parameters, details are given  
 114 in Section 3.1. The simulations concentrate on the early phase of an ELM-crash up to the  
 115 point where filaments start to form. The computations are carried out mostly on the HPC-FF  
 116 cluster located in Jülich, Germany. The `eta5` simulations with periodicity 1 and about 5500  
 117 Bezier elements require at least 102 compute nodes (8 cores and 24 GB of memory each) due  
 118 to memory requirements of the solver and take about ten thousand CPU hours to complete. The  
 119 `eta6` computation with 11000 Bezier elements is at the limit of what can be investigated with  
 120 JOREK on this machine.

### 121 3.1. Physical parameters

122 A typical ASDEX Upgrade H-mode discharge with type-I ELMs constitutes the basis of the  
 123 simulations: Geometry and profiles are taken from discharge 23221 at 4.7 seconds with a  
 124 plasma current of 1 MA, 8 MW of neutral beam injection heating and 1.5 MW of electron  
 125 cyclotron resonance heating. The equilibrium reconstruction with the CLISTE code [20, 21]  
 126 takes into account measured kinetic profiles. Source terms  $S_\rho$  and  $S_T$  and perpendicular diffu-  
 127 sivities  $D_\perp$  and  $K_\perp$  are adjusted such, that the equilibrium does not change significantly with  
 128 time. The core temperature is  $k_B T_{SI} = k_B (T_{e,SI} + T_{i,SI}) = 12.4 \text{ keV}$ . The safety-factor takes a  
 129 value of  $q(0) = 1$  in the plasma core and  $q(\Psi_N = 0.95) = 4.7$  close to the separatrix where  
 130  $\Psi_N = (\Psi - \Psi_{\text{axis}}) / (\Psi_{\text{separatrix}} - \Psi_{\text{axis}})$  denotes the normalized poloidal flux. A pure deuterium  
 131 plasma with a core density of  $6 \cdot 10^{19} \text{ m}^{-3}$  is assumed. The heat diffusion anisotropy,  $K_{||} / K_\perp$ ,  
 132 takes a value of  $7 \cdot 10^6$  at the separatrix.

133 The spatial resolution required for the simulation is, amongst others, determined by the resistive  
 134 skin depth  $\delta_{SI} = \sqrt{2\eta_{SI} / (\mu_0 \gamma_{SI})}$  which is about 6 mm in `eta6` simulations. As the spatial  
 135 resolution possible in the poloidal plane is limited by computational resources, realistic plasma  
 136 resistivities with a resistive skin depth of about 0.3 mm cannot be resolved (resolving spatial  
 137 scales smaller than the ion gyro-radius is of course not reasonable anyway in MHD-simulations).

138 The following data are used as inputs for the JOREK simulation:

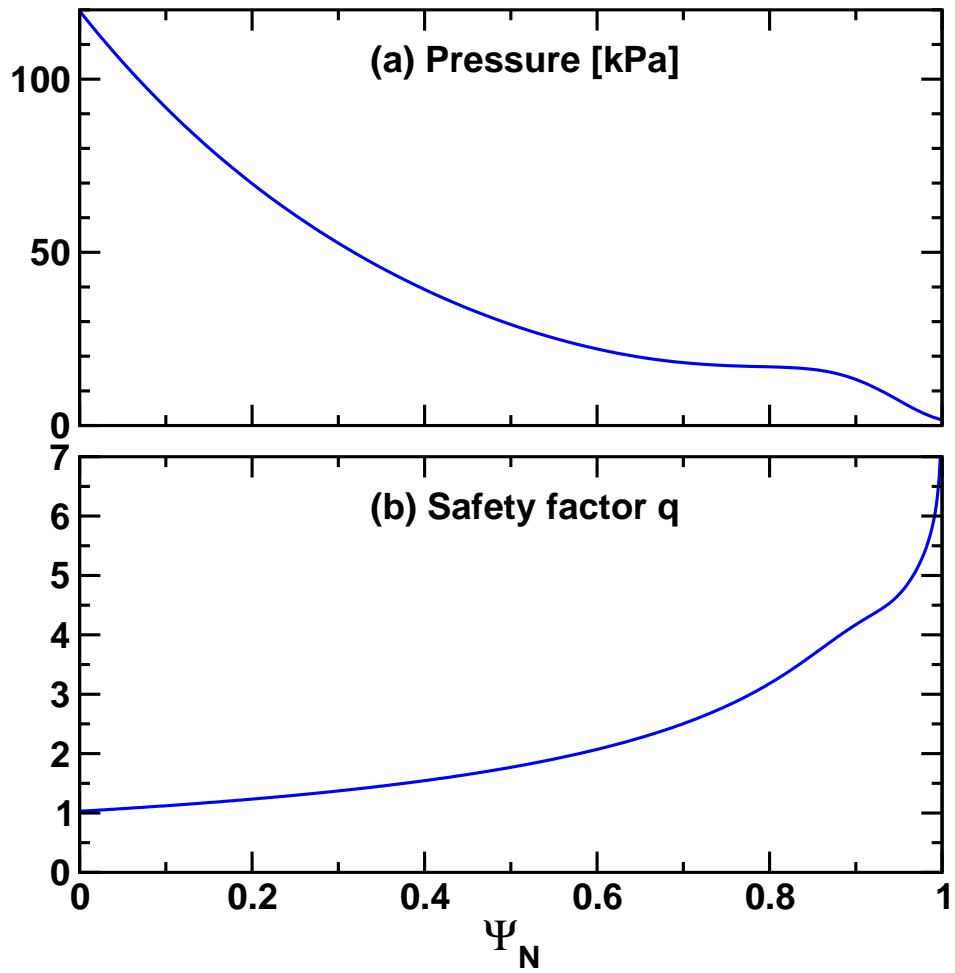


Figure 2: Profiles of (a) plasma pressure and (b) safety-factor are shown for the plasma equilibrium used in the simulations.

139 • From experimental measurements: Temperature and density profiles, and toroidal mag-  
140 netic field strength. The pressure profile is shown in Figure 2a.

141 • From CLISTE-equilibrium reconstruction based on experimental measurements:  $FF'$ -  
142 profile and the values of the poloidal Flux  $\Psi$  at the JOREK computational boundary. Here,  
143  $F = (2\pi/\mu_0) J_{\text{pol, SI}}$  is proportional to the poloidal plasma current,  $J_{\text{pol}}$ , and  $F' = dF/d\Psi$ .  
144 The  $q$ -profile of the equilibrium is shown in Figure 2b.

145 In JOREK simulations, the Grad-Shafranov equation is solved first based on these input param-  
146 eters. The equilibrium perfectly agrees with CLISTE ( $q$ -profile, flux surfaces, etc.). After that,  
147 an “equilibrium refinement” phase is required where the time-evolution equations are solved  
148 only for the  $n = 0$  mode, with very small time-steps that are gradually increased. This allows  
149 plasma flows to equilibrate [6]. Successively, the reduced MHD equations are evolved in time,  
150 taking into account some or many toroidal Fourier modes depending on the case considered.  
151 Instabilities then develop out of an initially very small random perturbation.

## 152 4. Simulation Results

153 In the following, the simulation results are described and analyzed. Section 4.1 addresses sim-  
154 ulations with low toroidal resolution, while Section 4.2 covers the situation at high toroidal  
155 resolution. In the succeeding Section 4.3, an attempt towards more realistic plasma resistivities  
156 is made. The simulation results are compared to experimental findings in Section 5.

### 157 4.1. Low Toroidal Resolution

158 This section provides simulation results for periodicity 8, where only the toroidal modes  $n = 0, 8,$   
159 and 16 are resolved. A ballooning-like exponentially growing mode located close to the plasma  
160 boundary develops at the low-field side. As seen in the energy diagnostics shown in Figure 3,  
161 the  $n = 8$  mode is linearly more unstable (growth rate  $\gamma_{\text{SI}} = 2.0 \times 10^5 \text{ s}^{-1}$ ) than the  $n = 16$   
162 mode ( $\gamma_{\text{SI}} \approx 1.5 \times 10^5 \text{ s}^{-1}$ ). Due to mode-coupling, the structure of the  $n = 16$  mode changes at  
163  $t = 284 \mu\text{s}$  in the simulation – the position of its maximum amplitude moves radially from the  
164  $q = 4$  to the adjacent  $q = 3.75$  resonant surface. Hereby, the growth rate of the  $n = 16$  mode  
165 increases significantly to  $\gamma_{\text{SI}} = 4.3 \times 10^5 \text{ s}^{-1}$  which is roughly the double  $n = 8$  growth rate. The  
166  $n = 8$  mode also remains dominant at the onset of non-linear mode saturation ( $t \approx 300 \mu\text{s}$ ).

167 The ballooning-structure that develops at the whole low-field side of the plasma is shown in  
168 Figure 4 for time point 298  $\mu\text{s}$  in the simulation. The “density-fingers” are very regular with

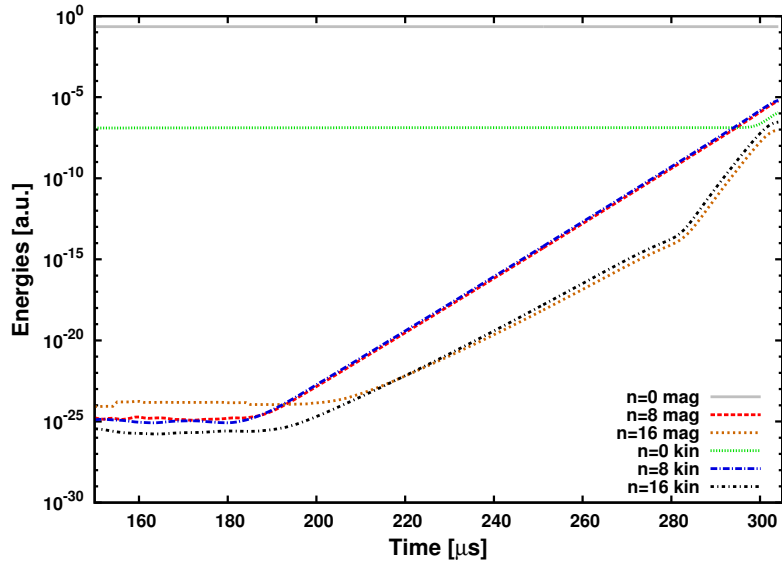


Figure 3: Time-traces of the magnetic and kinetic energies contained in the individual toroidal harmonics are plotted for the simulation with periodicity 8. The  $n = 8$  mode is linearly more unstable than the  $n = 16$  mode and also remains dominant when non-linear saturation sets in. Due to non-linear mode-interaction, the growth rate of the  $n = 16$  mode increases significantly at  $t = 284 \mu\text{s}$ . The  $n = 0$  magnetic energy is dominated by the toroidal magnetic field which is fixed in time as described in Section 2.1.

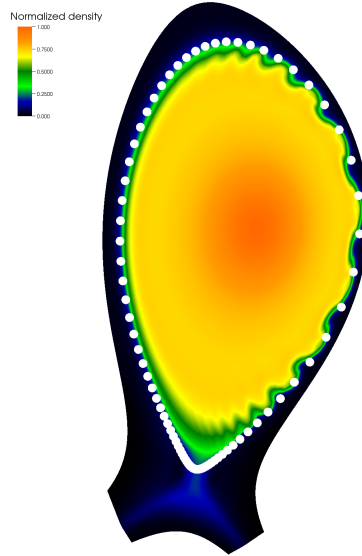


Figure 4: The density distribution with developing ballooning-structure in the simulation with periodicity 8 is shown at  $298 \mu\text{s}$ . Regular ballooning-structures are observed on the whole low-field side. All ballooning-fingers are roughly equally wide in poloidal direction in the straight-fieldline angle  $\theta^*$  (the white dots indicate equidistant distances in  $\theta^*$ ).

169 a poloidal size of about 15 – 20 cm at the outer midplane. The poloidal “compression” of the  
 170 structures in the vicinity of the lower (active) and the upper (inactive) X-points compared to the  
 171 outer midplane is a consequence of field-line stagnation – the poloidal width of the structures is  
 172 roughly constant in the straight-fieldline angle  $\theta^*$ . In Figure 4, this can be seen by comparing  
 173 the density fingers to the white dots which divide the poloidal circumference into equidistant  
 174 sections in  $\theta^*$ . When the exponentially growing perturbation gets visible in the density dis-  
 175 tribution, distortions start to build up which propagate into the vacuum region as finger-like  
 176 structures with significantly increased density due to the  $E \times B$  drift. Their radial velocity, mea-  
 177 sured by tracing the position at which the density equals 10 percent of the core density, increases  
 178 to about 3 km/s and saturates at that level. In the beginning, the density shows sinusoidal ex-  
 179 cursions of the density contours which grow over time (linear phase). As the instability grows  
 180 and non-linear saturation sets in (energy growth rates start to decrease), the density fingers de-  
 181 velop sub-structures. The changing structure also reflects in a different mode-spectrum, where  
 182 the  $n=16$  energies get closer to the  $n=8$  energies (Figure 3). The ideal-wall boundary condi-  
 183 tions contribute to the saturation of radial velocity when the distance between the mode and the  
 184 wall gets significantly smaller than its poloidal wave-length as mirror-currents build up that slow  
 185 down the mode-evolution.

## 186 4.2. High Toroidal Resolution

187 Now, the same setup as in the previous Section is considered at periodicity 1: All toroidal modes  
188 in the range  $n = 0$  to 16 are resolved. The comparison of simulations with different periodicities  
189 allows to identify effects caused by the coupling between toroidal modes.

190 Time-traces of the magnetic energies contained in each toroidal harmonic are shown in Figure 5.  
191 Linearly, the  $n = 10$  mode has the largest growth rate  $\gamma_{SI} \approx 2.0 \times 10^5 \text{ s}^{-1}$ . In a similar way as  
192 described for the  $n = 16$  mode in the previous Section, the initially very small growth rate of the  
193  $n = 1$  mode ( $\gamma_{SI} \approx 2 \times 10^4 \text{ s}^{-1}$ ) suddenly changes at  $t = 150 \mu\text{s}$  due to the non-linear interaction  
194 between the toroidal harmonics and becomes very large:  $\gamma_{SI} \approx 4 \times 10^5 \text{ s}^{-1}$ . In the non-linear  
195 phase of the mode, the  $n = 1$  perturbation reaches a similar magnetic energy as the  $n = 10$   
196 perturbation which remains dominant also at the beginning of non-linear saturation ( $t \approx 300 \mu\text{s}$ ).  
197 A first important effect that cannot be covered in simulations with low toroidal resolution (i.e.,  
198 high periodicity) is that low- $n$  modes can grow to large amplitudes non-linearly. The growth  
199 rate of the dominant mode ( $n = 10$  in our case) is not affected significantly by the toroidal  
200 mode-coupling. Also, the radial propagation velocity of the filaments into the vacuum region  
201 hardly changes compared to the case with low toroidal resolution: The filaments accelerate in  
202 the beginning and saturate at a velocity of about 3 km/s.

203 The developing density perturbation is shown in Figure 6. Also with high toroidal resolution,  
204 a ballooning-like structure is produced at the low-field side of the plasma. The poloidal size  
205 of the ballooning-fingers is around 10 – 12 cm at the midplane. In comparison to simulations  
206 with low toroidal resolution, these structures are a bit smaller. A significant difference becomes  
207 obvious when comparing Figures 4 and 6: Due to the mode-coupling, not all fingers grow to  
208 the same amplitude. A cluster of fingers can be seen that develops much stronger than the rest  
209 of the ballooning-structures. A strong localization of perturbations has also been observed in a  
210 ballooning-instability simulated with the BOUT code [22].

211 The localization of the perturbation becomes even more obvious when the magnetic footprint  
212 of the mode is considered. In Figure 7, the perturbation of the poloidal magnetic flux is plotted  
213 for simulations with different periodicities. Clearly, the localization of the mode can only be  
214 described correctly in simulations with periodicity 1. Figure 8 shows the perturbation of the  
215 poloidal flux at the outboard midplane versus the toroidal angle.

216 The perturbation is already localized in the linear phase of the mode. A qualitative change  
217 between the linear and the non-linear phases is shown in Figure 9, where the current perturbation  
218 is plotted for two different time-frames in the simulation with periodicity 1. In the non-linear  
219 phase where the ballooning-fingers become visible in the density perturbation, the previously  
220 alternating current filaments merge at the position of the separatrix around the outer midplane.  
221 Large areas with positive respectively negative currents are created.

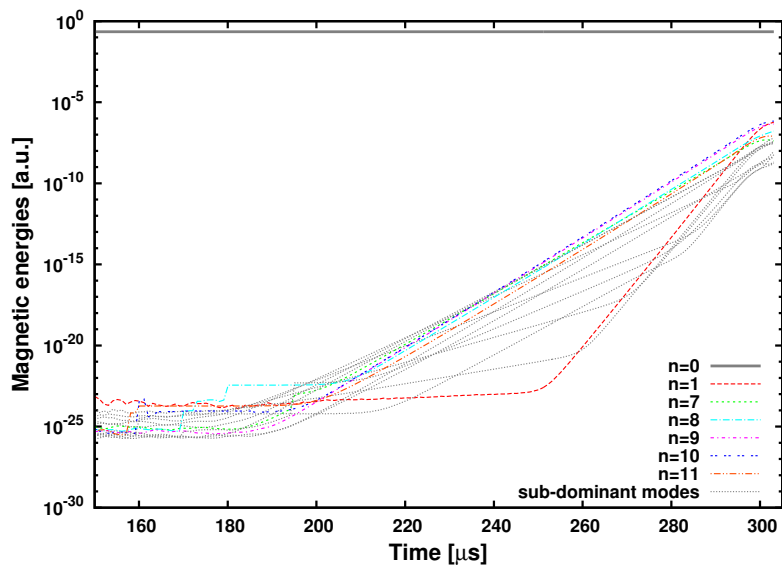


Figure 5: Time-traces of the magnetic energies contained in the individual toroidal modes are shown for the simulation with periodicity 1. For clarity, kinetic energies are omitted and sub-dominant modes are only indicated by dotted gray lines. It is remarkable that the  $n = 1$  mode reaches a comparable energy level at the onset of non-linear saturation as the  $n = 10$  mode, which is the linearly most unstable mode.

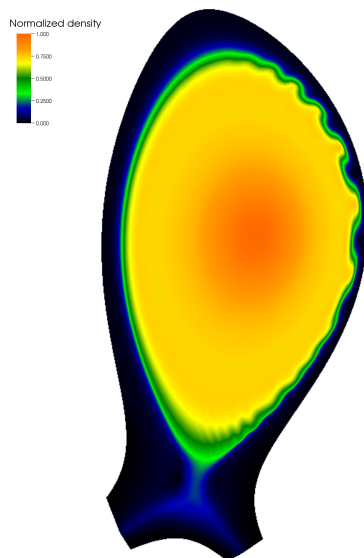


Figure 6: The density-perturbation observed in the simulation with periodicity 1 is plotted at 294  $\mu\text{s}$ . The ballooning-structures become less regular and perturbations are strong only within a localized region. In the cross-section shown, this region is located on the upper low-field side.

222 The strongest perturbations of all physical quantities are localized in a flux-tube like region  
 223 which extends from the vicinity of the lower active X-point along magnetic field lines to the  
 224 vicinity of the upper inactive X-point (compare Figure 7). The perturbations are strongest around  
 225 the midplane. As an exception,  $v_{\parallel}$  is perturbed especially around the end-points of this flux-tube,  
 226 a consequence of field-line stagnation close to the X-points. However, the radial perturbation  
 227 positions differ as shown in Figure 10. It can be seen, that the strongest perturbations of the  
 228 magnetic quantities  $\Psi$  and  $j$  are located in the region of strong plasma current, while the kinetic  
 229 quantities are perturbed further outwards in the region of strong pressure gradients.

### 230 4.3. Towards more Realistic Resistivities

231 This Section briefly shows results for simulations with the plasma viscosity and resistivity re-  
 232 duced by a factor of 10 (`eta6` cases) compared to the simulations shown above. To be able to  
 233 resolve these more realistic parameters, the number of 2D Bezier elements in the poloidal plane  
 234 was increased by a factor of two. These simulations need to be considered with care as the most  
 235 unstable mode is  $n = 13$  while we do not take into account mode numbers beyond  $n = 16$  for  
 236 computational reasons.

237 It can be seen that a strong localization of the perturbations is observed at periodicity 1 as  
 238 in the `eta5`-cases. This is shown for the perturbation of the poloidal flux in Figure 11. In

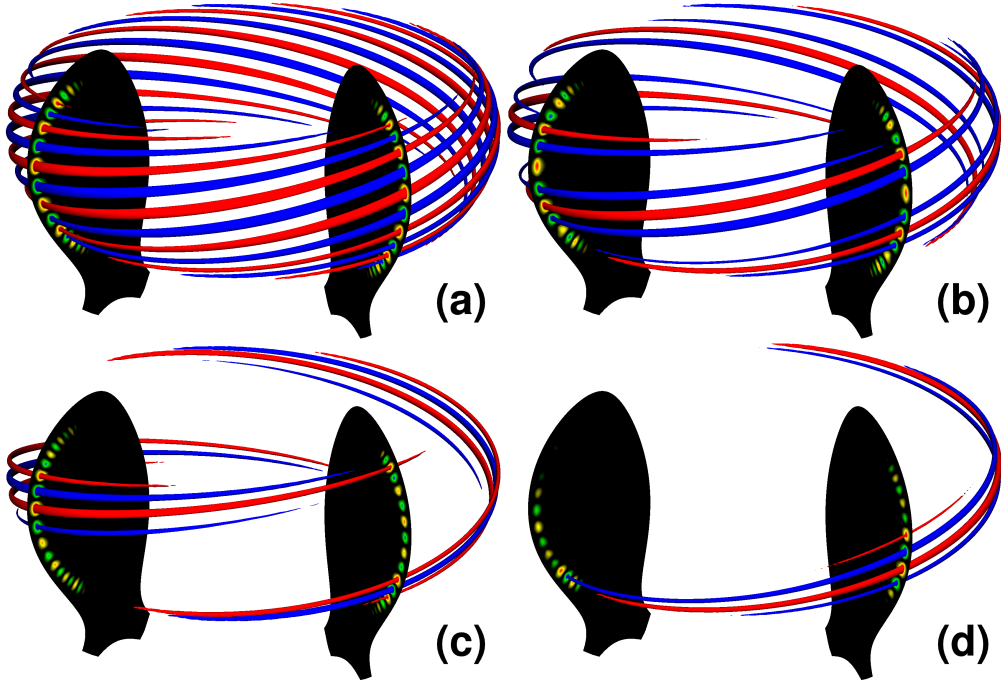


Figure 7: Contours of the poloidal flux perturbation are shown for simulations with (a) periodicity 8, (b) 4, (c) 2, and (d) 1, respectively. The red and blue contours are plotted at the surfaces corresponding to the perturbed poloidal flux values  $\tilde{\Psi}_{\text{red/blue}} = \pm 0.7 \cdot (|\tilde{\Psi}_{\text{min}}| + \tilde{\Psi}_{\text{max}})/2$ . Here,  $\tilde{\Psi}_{\text{min}}$  and  $\tilde{\Psi}_{\text{max}}$  denote the strongest negative positive perturbation values, respectively. At lower periodicities, the perturbation steadily gets more localized.

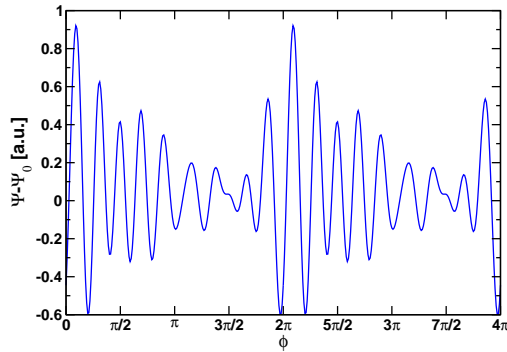


Figure 8: The perturbation of the poloidal flux at the outboard midplane is shown for the simulation with periodicity 1 versus the toroidal angle for two transits around the torus. The perturbation amplitude shows a strong toroidal variation equivalent to a localization of the perturbation to  $\Delta\phi \approx 3$  rad (f.w.h.m.). As equilibrium, boundary conditions, and sources are completely axi-symmetric, the localization position is essentially arbitrary which proves to be true when looking at a set of different simulations.

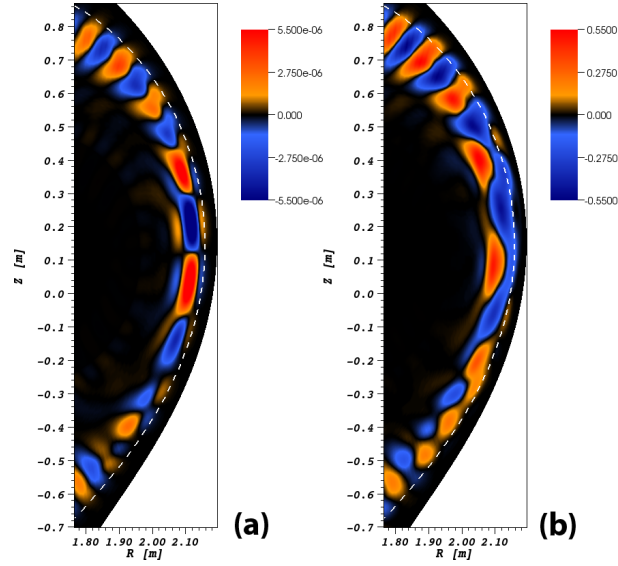


Figure 9: The current perturbation at the plasma edge is shown for the simulation with periodicity 1 in the (a) linear (240  $\mu$ s) and (b) non-linear phases (300  $\mu$ s). In the non-linear phase, large regions with positive respectively negative current (this cross-section) form at the separatrix (dashed line) around the midplane.

239 contrast to the  $\eta_{a5}$ -simulations, the perturbation maximum is not located around the midplane  
 240 but more towards the top and bottom regions of the low-field side. This distribution of the  
 241 flux-perturbation is not an artifact caused by cutting toroidally at  $n = 16$ : A simulation with  
 242 periodicity 2 was carried out in which the toroidal modes  $n = 0, 2, \dots, 20, 22$  are resolved, where  
 243 the strongest perturbation of the poloidal flux is not observed at the midplane but above and  
 244 below it, as well.

245 At ASDEX Upgrade, an off-midplane mode-structure has recently been observed in the tem-  
 246 perature using ECE-Imaging [23]. In our simulations, the perturbation maximum of the kinetic  
 247 quantities is, however, located around the midplane. This is a consequence of the comparably  
 248 large plasma resistivities in our simulations which allow magnetic and kinetic quantities to de-  
 249 couple. At smaller resistivities, which we cannot resolve at present, also the kinetic quantities  
 250 might show an off-midplane behavior.

## 251 5. Comparison to Experiments

252 In this Section, some properties of the simulated edge instabilities are compared to experimental  
 253 observations. This shows that important aspects of the early phase of edge localized modes

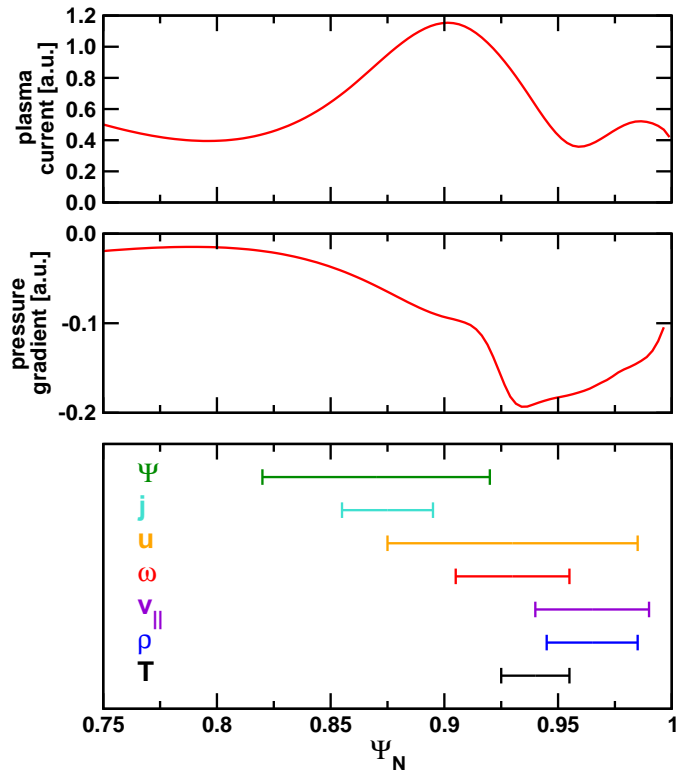


Figure 10: For the simulation with periodicity 1, the radial positions of the strongest perturbations are shown at  $t = 300 \mu\text{s}$  for the seven physical variables and are compared to profiles of the plasma current and the pressure gradient.

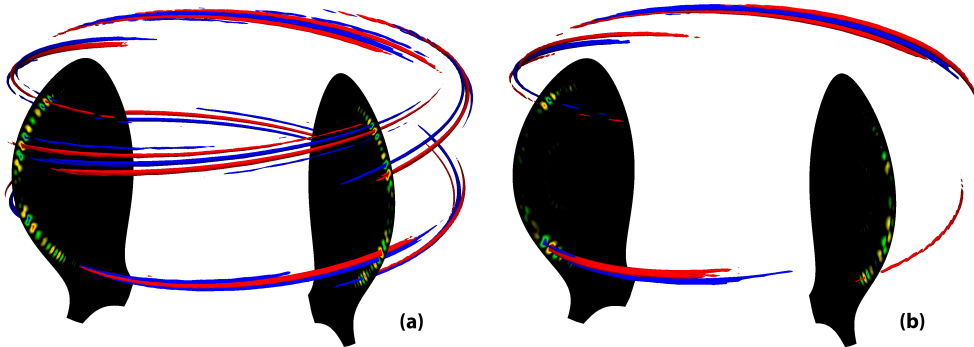


Figure 11: For simulations with (a) periodicity 2 respectively (b) 1 where the plasma resistivity and viscosity is reduced by a factor of 10 compared to the simulations presented above, the poloidal flux perturbation is shown analogously to Figure 7. A strong localization of perturbations is observed in these simulations as well.

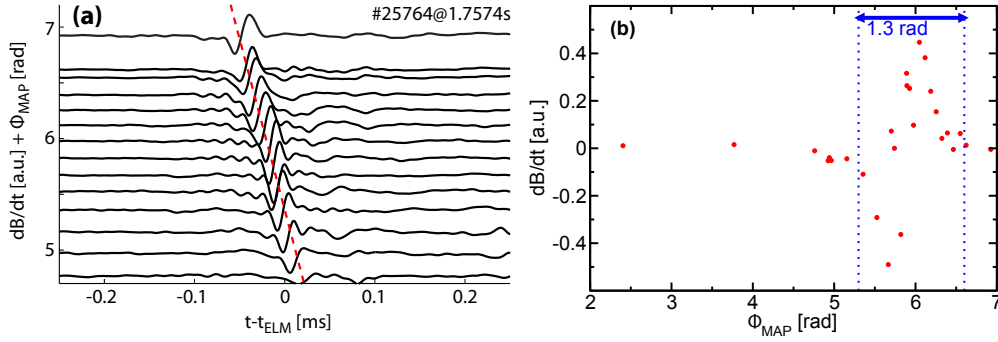


Figure 12: **(a)** Magnetic signals from selected Mirnov-coils are shown for a strongly localized solitary magnetic perturbation in ASDEX Upgrade as in Reference [24]. All measurement locations are mapped to a common toroidal angle  $\phi_{\text{MAP}}$  via field-line tracing. The magnetic perturbation propagates with constant toroidal velocity in the electron diamagnetic drift direction in the lab-frame as indicated by the red dashed line. The onset time of the erosion of pedestal temperature and density profiles is denoted  $t_{\text{ELM}}$ . **(b)** The time-derivative of the magnetic field measured by Mirnov coils is plotted versus the toroidal mapping angle  $\phi_{\text{MAP}}$  at  $t - t_{\text{ELM}} = -0.03$  ms. The solitary magnetic perturbation is localized to  $\Delta\phi \approx 1.2$  rad.

254 are well described by the reduced MHD model. More detailed comparisons between JOREK  
 255 simulations of complete ELM crashes and experimental measurements at ASDEX Upgrade are  
 256 planned for the future (e.g., evolution of pedestal gradients, detachment of filaments, heat-flux  
 257 patterns at divertor plates).

258 The poloidal flux perturbation from the simulation with periodicity 1 shown in Figure 8 ex-  
 259 hibits a toroidal localization: Large perturbation amplitudes are localized to a region of about  
 260  $\Delta\phi \approx 3$  rad. Thus, the modes we observe in our simulations of the early ELM phase when sim-  
 261 ulating the full torus (periodicity 1) exhibit a similar magnetic structure as so-called solitary  
 262 magnetic perturbations recently discovered at the ELM onset in ASDEX Upgrade and described  
 263 in great detail in Reference [24]. From the systematic analysis of a large number of ELM crashes,  
 264 a continuous distribution of the mode solitariness was reported between cases with a very pro-  
 265 nounced toroidal localization (an example is shown in Figure 12) and cases with a magnetic  
 266 perturbation strength that is toroidally virtually uniform. The toroidal localization observed in  
 267 our simulations (localized to  $\Delta\phi \approx 3$  rad) is less pronounced than the extreme example of Fig-  
 268 ure 12b with  $\Delta\phi \approx 1.3$  rad. A direct comparison is planned for the future making use of a virtual  
 269 magnetic diagnostic which determines magnetic signals from the simulations at the same posi-  
 270 tions as the Mirnov coils. Toroidally asymmetric structures at ELMs are also described from  
 271 experimental observations in References [25–28]. In analytical calculations, localized instabil-  
 272 ities were also reported by Wilson et.al. [29]. These “explosive ballooning” instabilities grow  
 273 much faster non-linearly than linearly and a poloidal narrowing of the instability in the non-  
 274 linear phase is reported. Both features are not observed in the simulated edge instabilities which

275 indicates that different mechanisms are responsible for the localization in our simulations.

276 The dominant toroidal mode-number turns out to be 10 in the simulations. With the plasma  
277 resistivity reduced towards more realistic values, the dominant mode number shifts towards 13.  
278 This is in quite good agreement to experimental findings in the tokamaks ASDEX Upgrade and  
279 MAST for type-I ELMs, where mode-numbers of 8 – 24 were observed in energy deposition  
280 patterns [27], around 15 was found from measurements with the midplane manipulator and  
281 visible-light imaging [30], and mode numbers of  $18 \pm 4$  have been obtained for the onset of the  
282 ELM-crash using ECE-Imaging [23]. Uncertainties in our simulations come from the limited  
283 poloidal resolution and the neglect of diamagnetic stabilization as discussed in Section 3.

284 Low- $n$  modes gain large amounts of energy non-linearly in our simulations with periodicity 1.  
285 This allows them to interact much more efficiently with core-MHD modes like tearing modes  
286 which typically also feature low toroidal mode numbers like 1 or 2. Indeed, there is experimen-  
287 tal evidence from the DIII-D tokamak that ELMs are an important triggering mechanism for  
288 neoclassical tearing modes [31].

289 The poloidal extent of filaments on the outer midplane observed in simulations with high toroidal  
290 resolution is around 10 – 12 cm. Measurements in ASDEX Upgrade and MAST revealed fila-  
291 ment sizes perpendicular to the field lines of 5 – 10 cm [30]. For ASDEX Upgrade, perpendic-  
292 ular and poloidal filament sizes are equivalent due to the small field-line pitch-angle such that  
293 simulation results and experimental observations show good agreement here as well.

294 In the simulations, the radial velocity of the developing finger structures saturates at about  
295 3 km/s after an initial acceleration. This corresponds to a distribution of the radial filament  
296 speed with an upper limit of 3 km/s. This velocity depends on the stability of the initial equilib-  
297 rium. The unrealistically large values for the plasma resistivity might lead to an over-estimation  
298 of the filament speeds, while the ideal-wall boundary conditions tend to reduce the radial veloc-  
299 ity. In experimental measurements, the radial filament speed is found to be distributed around  
300 1 km/s in ASDEX Upgrade [32, 33]. Filament speeds faster than 2 km/s occur in 20% of the  
301 cases in both References and almost no filaments faster than 3 km/s are observed. Hence, radial  
302 filament speeds in simulations and experimental measurements seem to agree reasonably well.

303 In the magnetic quantities, an off-midplane mode-structure is observed in the simulations with  
304 lower plasma resistivity ( $\eta_{a6}$  simulations). As the resistivity is still unrealistically large in  
305 these simulations, magnetic and kinetic quantities are decoupled such that the strongest perturba-  
306 tion of the temperature is located at the midplane. Still, this might be related to the off-midplane  
307 structures observed by ECE-Imaging in ASDEX Upgrade [23].

## 308 **6. Conclusions and Outlook**

309 Exponentially growing ballooning-like modes have been simulated with the reduced-MHD ver-  
310 sion of the non-linear MHD code JOREK in the geometry and using the profiles of a typical  
311 ASDEX Upgrade H-mode discharge. Dominant toroidal mode numbers, poloidal filament sizes,  
312 and radial filament-propagation speeds of these instabilities are in good agreement with exper-  
313 imental observations for type-I ELMs in ASDEX Upgrade. At sufficient toroidal resolution,  
314 perturbations show a pronounced toroidal and poloidal localization which is compatible with  
315 solitary magnetic perturbations recently discovered in ASDEX Upgrade. In some cases, the  
316 perturbation of the magnetic flux is stronger at the top and bottom low-field side than at the  
317 midplane. Presumably due to a decoupling of magnetic and kinetic quantities caused by the un-  
318 realistically large plasma resistivity, density and temperature perturbations are always localized  
319 on the midplane of the low-field side. Strong perturbations in the low- $n$  modes are triggered  
320 non-linearly in the simulations with periodicity 1 and might explain the strong interaction of  
321 ELMs with core-MHD modes like neoclassical tearing modes observed in some experiments.

322 While this work concentrates on the early phase of an ELM, further studies are planned to com-  
323 pare the simulation of a full ELM crash to experimental observations requiring a more sophisti-  
324 cated modeling of the scrape-off layer. Simulations of a full ELM cycle will also be attempted.  
325 Future numerical improvements and increased computational resources will be used to advance  
326 our investigations towards more realistic plasma parameters while keeping high toroidal resolu-  
327 tions.

## 328 **7. Acknowledgments**

329 The simulations were mostly carried out on the HPC-FF computing cluster in Jülich, Ger-  
330 many. One of the authors (K.L.) would like to acknowledge the support by the Austrian Sci-  
331 ence Fund (FWF) under grant No. P19901. Additionally, the authors would like to thank Erika  
332 Strumberger and Mike Dunne for their help with the plasma equilibrium reconstruction and  
333 Klaus Reuter for assistance with visualizations.

## 334 **A. Derivation of the Induction Equation**

The reduced MHD equations implemented in the JOREK code can be derived following Refer-  
ence [16]. For the induction equation, this is shown in the following. The starting points are the

well-known expression for the electric field in the MHD approximation,

$$\mathbf{E} = -\mathbf{v} \times \mathbf{B} + \eta \mathbf{j} \quad (10)$$

and the Maxwell-Faraday law expressed in the vector potential  $\mathbf{A}$ ,

$$\frac{\partial \mathbf{A}}{\partial t} = -\mathbf{E} - F_0 \nabla u. \quad (11)$$

Inserting (10) into (11) and multiplying it with the toroidal unity vector  $\hat{\mathbf{e}}_\phi$  yields

$$\frac{\partial \Psi}{\partial t} = \eta j + (\mathbf{v} \times \mathbf{B}) \cdot \hat{\mathbf{e}}_\phi - F_0 \nabla u \cdot \hat{\mathbf{e}}_\phi, \quad (12)$$

where the poloidal flux is identified as the major radius times the toroidal component of the vector potential,  $\Psi \equiv R \mathbf{A} \cdot \hat{\mathbf{e}}_\phi$ , and  $j = -\mathbf{j} \cdot \hat{\mathbf{e}}_\phi$  denotes the toroidal plasma current. Using Equations (8) and (9), this can be written as

$$\frac{\partial \Psi}{\partial t} = \eta j - R[u, \Psi] - F_0 \frac{\partial u}{\partial \phi}, \quad (13)$$

335 which is the induction equation (Equation (3)) solved in the JOREK reduced MHD model with  
 336 the Poisson bracket  $[u, \Psi] = \frac{\partial u}{\partial R} \frac{\partial \Psi}{\partial Z} - \frac{\partial u}{\partial Z} \frac{\partial \Psi}{\partial R}$ . In the last step, the reduced MHD approximation to  
 337 first order in  $\varepsilon = \nabla_{\parallel} \Psi / \nabla_{\perp} \Psi \ll 1$  yielding  $\mathbf{v}_{\text{pol}} \approx \mathbf{v}_{\perp}$  was applied.

338 The poloidal components of Equation (11), obtained by applying the operator  $\hat{\mathbf{e}}_\phi \times$  to this equa-  
 339 tion, yield a definition equation for the poloidal velocity (see poloidal components of Equa-  
 340 tion (8)) in which  $u$  can be identified as the poloidal velocity stream function. In this set of  
 341 equations,  $u$  also acts as electric potential (except for a constant factor  $F_0$ ).

342 Galilei-invariance of the induction equation (Equation (11)) is not obvious at first glance. How-  
 343 ever, the proof is straightforward when taking into account that the scalar potential  $\phi = F_0 u$  is  
 344 modified according to  $\phi \rightarrow \phi - \mathbf{v}_0 \cdot \mathbf{A}$  under the transformation  $\mathbf{v} \rightarrow \mathbf{v} - \mathbf{v}_0$  while the vector po-  
 345 tential remains unchanged (non-relativistic limit). In the large aspect-ratio limit, it can also be  
 346 shown easily that the reduced-MHD induction equation (Equation (13)) is invariant to a trans-  
 347 formation  $\mathbf{v} \rightarrow \mathbf{v} - \mathbf{v}_z$  with  $z$  along the cylinder axis, as the scalar potential transforms according  
 348 to  $\phi \rightarrow \phi - v_z \Psi$ .

## 349 References

- 350 [1] A Loarte, G Saibene, R Sartori, D Campbell, M Becoulet, L Horton, T Eich, A Herrmann,  
 351 G Matthews, N Asakura, A Chankin, A Leonard, G Porter, G Federici, G Janeschitz,  
 352 M Shimada, and M Sugihara. Characteristics of type I ELM energy and particle losses

- 353 in existing devices and their extrapolation to ITER. *Plasma Physics and Controlled Fu-*  
354 *sion*, 45(9):1549, 2003. URL [http://stacks.iop.org/0741-3335/45/i=9/](http://stacks.iop.org/0741-3335/45/i=9/a=302)  
355 [a=302](http://stacks.iop.org/0741-3335/45/i=9/a=302).
- 356 [2] N. Klimov, V. Podkovyrov, A. Zhitlukhin, D. Kovalenko, J. Linke, G. Pintsuk,  
357 I. Landman, S. Pestchanyi, B. Bazylev, G. Janeschitz, A. Loarte, M. Merola,  
358 T. Hirai, G. Federici, B. Riccardi, I. Mazul, R. Giniyatulin, L. Khimchenko, and  
359 V. Koidan. Experimental study of PFCs erosion and eroded material deposi-  
360 tion under ITER-like transient loads at the plasma gun facility QSPA-T. *Jour-*  
361 *nal of Nuclear Materials*, 415(1, Supplement):S59 – S64, 2011. ISSN 0022-3115.  
362 doi:10.1016/j.jnucmat.2011.01.013. URL [http://www.sciencedirect.com/](http://www.sciencedirect.com/science/article/pii/S0022311511000250)  
363 [science/article/pii/S0022311511000250](http://www.sciencedirect.com/science/article/pii/S0022311511000250). <ce:title>Proceedings of the 19th  
364 International Conference on Plasma-Surface Interactions in Controlled Fusion</ce:title>.
- 365 [3] G.T.A. Huysmans and O. Czarny. MHD stability in X-point geometry: simulation  
366 of ELMs. *Nuclear Fusion*, 47(7):659, 2007. URL [http://stacks.iop.org/](http://stacks.iop.org/0029-5515/47/i=7/a=016)  
367 [0029-5515/47/i=7/a=016](http://stacks.iop.org/0029-5515/47/i=7/a=016).
- 368 [4] G.T.A. Huysmans, R. Abgrall, M. Becoulet, R. Huart, B. Nkonga, S. Pamela, E. van der  
369 Plas, and P. Ramet. Non-linear MHD simulations of ELMs. In *Proceedings of the 35th*  
370 *EPS Conference on Plasma Physics*, pages P-2.065, Hersonissos, 2008. URL [epsppd.](http://epsppd.epfl.ch/Hersonissos/pdf/P2_065.pdf)  
371 [epfl.ch/Hersonissos/pdf/P2\\_065.pdf](http://epsppd.epfl.ch/Hersonissos/pdf/P2_065.pdf).
- 372 [5] G T A Huysmans, S Pamela, E van der Plas, and P Ramet. Non-linear MHD simulations  
373 of edge localized modes (ELMs). *Plasma Physics and Controlled Fusion*, 51(12):124012,  
374 2009. URL <http://stacks.iop.org/0741-3335/51/i=12/a=124012>.
- 375 [6] S Pamela, G Huysmans, and S Benkadda. Influence of poloidal equilibrium rotation  
376 in MHD simulations of edge-localized modes. *Plasma Physics and Controlled Fusion*,  
377 52(7):075006, 2010. URL [http://stacks.iop.org/0741-3335/52/i=7/a=](http://stacks.iop.org/0741-3335/52/i=7/a=075006)  
378 [075006](http://stacks.iop.org/0741-3335/52/i=7/a=075006).
- 379 [7] G. Huysmans, S. Pamela, M. Beurskens, M. Becoulet, and E. van der Plas. Non-linear  
380 MHD simulation of natural and pellet triggered ELMs. In *Proceedings of th 23rd IAEA*  
381 *Fusion Energy Conference*, Daejeon, South Korea, 2010.
- 382 [8] S J P Pamela, G T A Huysmans, M N A Beurskens, S Devaux, T Eich, S Benkadda, and  
383 JET EFDA contributors. Nonlinear MHD simulations of edge-localized-modes in JET.  
384 *Plasma Physics and Controlled Fusion*, 53(5):054014, 2011. URL [http://stacks.](http://stacks.iop.org/0741-3335/53/i=5/a=054014)  
385 [iop.org/0741-3335/53/i=5/a=054014](http://stacks.iop.org/0741-3335/53/i=5/a=054014).
- 386 [9] M. Hölzl, S. Günter, and ASDEX Upgrade Team. Reduced-MHD simulations of edge  
387 localized modes in ASDEX Upgrade (P2.078). In *Proceedings of the 38th EPS Conference*  
388 *on Plasma Physics*, Strasbourg, France, 2011.
- 389 [10] B D Dudson, X Q Xu, M V Umansky, H R Wilson, and P B Snyder. Simulation of edge  
390 localized modes using BOUT++. *Plasma Physics and Controlled Fusion*, 53(5):054005,  
391 2011. URL <http://stacks.iop.org/0741-3335/53/i=5/a=054005>.

- 392 [11] A Y Pankin, G Bateman, D P Brennan, A H Kritz, S Kruger, P B Snyder, C Sovinec,  
393 and the NIMROD team. Modelling of ELM dynamics for DIII-D and ITER. *Plasma*  
394 *Physics and Controlled Fusion*, 49(7):S63, 2007. URL [http://stacks.iop.org/  
395 0741-3335/49/i=7/a=S04](http://stacks.iop.org/0741-3335/49/i=7/a=S04).
- 396 [12] L. E. Sugiyama and H. R. Strauss. Magnetic X-points, edge localized modes, and  
397 stochasticity. *Physics of Plasmas*, 17(6):062505, 2010. doi:10.1063/1.3449301. URL  
398 <http://link.aip.org/link/?PHP/17/062505/1>.
- 399 [13] O Czarny and G Huysmans. Bezier surfaces and finite elements for MHD simula-  
400 tions. *Journal of Computational Physics*, 227(16):7423 – 7445, 2008. ISSN 0021-  
401 9991. doi:10.1016/j.jcp.2008.04.001. URL [http://www.sciencedirect.com/  
402 science/article/pii/S0021999108002118](http://www.sciencedirect.com/science/article/pii/S0021999108002118).
- 403 [14] A. Hermann. Special issue: ASDEX Upgrade. *Fusion Science and Technology*, 44(3),  
404 2003. URL [http://www.new.ans.org/pubs/journals/fst/v\\_44:3](http://www.new.ans.org/pubs/journals/fst/v_44:3).
- 405 [15] E Wolfrum, M Bernert, J E Boom, A Burckhart, I G J Classen, G D Conway, T Eich,  
406 R Fischer, A Gude, A Herrmann, N C Luhmann Jr, M Maraschek, R McDermott, H K  
407 Park, T Puetterich, J Vicente, B Wieland, M Willensdorfer, and the ASDEX Upgrade  
408 Team. Characterization of edge profiles and fluctuations in discharges with type-II and  
409 nitrogen-mitigated edge localized modes in ASDEX Upgrade. *Plasma Physics and Con-  
410 trolled Fusion*, 53(8):085026, 2011. URL [http://stacks.iop.org/0741-3335/  
411 53/i=8/a=085026](http://stacks.iop.org/0741-3335/53/i=8/a=085026).
- 412 [16] H. R. Strauss. Reduced mhd in nearly potential magnetic fields. *Journal of Plasma Physics*,  
413 57(1):83–87, 1997. doi:10.1017/S0022377896005296.
- 414 [17] P. C. Stangeby and A. V. Chankin. The ion velocity (Bohm–Chodura) boundary condition  
415 at the entrance to the magnetic presheath in the presence of diamagnetic and  $E \times B$  drifts  
416 in the scrape-off layer. *Physics of Plasmas*, 2(3):707–715, 1995. doi:10.1063/1.871421.  
417 URL <http://link.aip.org/link/?PHP/2/707/1>.
- 418 [18] Charles Hirsch. *Numerical Computation of Internal and External Flows, Volume 1, Fun-  
419 damentals of Numerical Discretization*. Wiley, 1989. ISBN 978-0-471-92385-5.
- 420 [19] Website of PASTIX. URL <https://gforge.inria.fr/projects/pastix/>.
- 421 [20] P. J. McCarthy, P. Martin, and W. Schneider. The CLISTE interpretive equilibrium  
422 code. Technical Report IPP-Report 5/85, Max-Planck-Institut für Plasmaphysik, Boltz-  
423 mannstraße 2, 85748 Garching, Germany, 1999. URL [http://edoc.mpg.de/  
424 display.epl?mode=doc&id=413804&col=33&grp=1311#cb](http://edoc.mpg.de/display.epl?mode=doc&id=413804&col=33&grp=1311#cb).
- 425 [21] P. J. McCarthy. Analytical solutions to the Grad-Shafranov equation for toka-  
426 mak equilibrium with dissimilar source functions. *Phys. Plasmas*, 6(9):3554, 1999.  
427 doi:10.1063/1.873630.

- 428 [22] P. B. Snyder, H. R. Wilson, and X. Q. Xu. Progress in the peeling-ballooning model of  
 429 edge localized modes: Numerical studies of nonlinear dynamics. *Physics of Plasmas*,  
 430 12(5):056115, 2005. doi:10.1063/1.1873792. URL [http://link.aip.org/link/  
 431 ?PHP/12/056115/1](http://link.aip.org/link/?PHP/12/056115/1).
- 432 [23] J.E. Boom, I.G.J. Classen, P.C. de Vries, T. Eich, E. Wolfrum, W. Suttrop, R.P. Wenninger,  
 433 A.J.H. DonnÄl, B.J. Tobias, C.W. Domier, N.C. Luhmann Jr, H.K. Park, and the AS-  
 434 DEX Upgrade Team. 2D ECE measurements of type-I edge localized modes at ASDEX  
 435 Upgrade. *Nuclear Fusion*, 51(10):103039, 2011. URL [http://stacks.iop.org/  
 436 0029-5515/51/i=10/a=103039](http://stacks.iop.org/0029-5515/51/i=10/a=103039).
- 437 [24] R P Wenninger, H Zohm, J Boom, T Eich, M Garcia-Munoz, M Hoelzl, T Lunt,  
 438 M Maraschek, H W Mueller, F Sommer, E Viezzer, and the ASDEX Upgrade Team. Soli-  
 439 tary magnetic perturbations at the ELM onset. *Nuclear Fusion*. accepted.
- 440 [25] H. Reimerdes, A. Pochelon, and W. Suttrop. Toroidally asymmetric ELM precursors  
 441 in TCV. *Nuclear Fusion*, 38(3):319, 1998. URL [http://stacks.iop.org/  
 442 0029-5515/38/i=3/a=101](http://stacks.iop.org/0029-5515/38/i=3/a=101).
- 443 [26] M Bécoulet, G Huysmans, Y Sarazin, X Garbet, Ph Ghendrih, F Rimini, E Joffrin,  
 444 X Litaudon, P Monier-Garbet, J-M Ané, P Thomas, A Grosman, V Parail, H Wilson,  
 445 P Lomas, P deVries, K-D Zastrow, G F Matthews, J Lonroth, S Gerasimov, S Shara-  
 446 pov, M Gryaznevich, G Counsell, A Kirk, M Valovic, R Buttery, A Loarte, G Saibene,  
 447 R Sartori, A Leonard, P Snyder, L L Lao, P Gohil, T E Evans, R A Moyer, Y Kamada,  
 448 A Chankin, N Oyama, T Hatae, N Asakura, O Tudisco, E Giovannozzi, F Crisanti, C P  
 449 Perez, H R Koslowski, T Eich, A Sips, L Horton, A Hermann, P Lang, J Stober, W Sut-  
 450 trop, P Beyer, S Saarelma, and Contributors to JET-EFDA Workprogramme. Edge local-  
 451 ized mode physics and operational aspects in tokamaks. *Plasma Physics and Controlled  
 452 Fusion*, 45(12A):A93, 2003. URL [http://stacks.iop.org/0741-3335/45/i=  
 453 12A/a=007](http://stacks.iop.org/0741-3335/45/i=12A/a=007).
- 454 [27] T. Eich, A. Herrmann, and J. Neuhauser. Nonaxisymmetric energy deposition pattern on  
 455 ASDEX Upgrade divertor target plates during type-I edge-localized modes. *Phys. Rev.  
 456 Lett.*, 91:195003, Nov 2003. doi:10.1103/PhysRevLett.91.195003.
- 457 [28] V.I.V. Bobkov, M. Becoulet, T. Blackman, J. Brzozowski, C. Challis, S. Gerasimov, P.U.  
 458 Lamalle, M. Maraschek, M.-L. Mayoral, I. Monakhov, J.-M. Noterdaeme, G. Saibene,  
 459 A. Walden, P. Wouters, ASDEX Upgrade Team, and JET-EFDA contributors. Studies of  
 460 ELM toroidal asymmetry using ICRF antennas at JET and ASDEX Upgrade. In *Euro-  
 461 physics Conference Abstracts*, volume 28G, 2004. URL [http://epsppd.epfl.ch/  
 462 London/pdf/P1\\_141.pdf](http://epsppd.epfl.ch/London/pdf/P1_141.pdf).
- 463 [29] H. R. Wilson and S. C. Cowley. Theory for explosive ideal magnetohy-  
 464 drodynamic instabilities in plasmas. *Phys. Rev. Lett.*, 92:175006, Apr 2004.  
 465 doi:10.1103/PhysRevLett.92.175006. URL [http://link.aps.org/doi/10.  
 466 1103/PhysRevLett.92.175006](http://link.aps.org/doi/10.1103/PhysRevLett.92.175006).

- 467 [30] A Kirk, T Eich, A Herrmann, H W Muller, L D Horton, G F Counsell, M Price, V Rohde,  
468 V Bobkov, B Kurzan, J Neuhauser, H Wilson, the ASDEX Upgrade, and MAST Teams.  
469 The spatial structure of type-I ELMs at the mid-plane in ASDEX Upgrade and a compari-  
470 son with data from MAST. *Plasma Physics and Controlled Fusion*, 47(7):995, 2005. URL  
471 <http://stacks.iop.org/0741-3335/47/i=7/a=003>.
- 472 [31] O. Sauter, R. J. La Haye, Z. Chang, D. A. Gates, Y. Kamada, H. Zohm, A. Bondeson,  
473 D. Boucher, J. D. Callen, M. S. Chu, T. A. Gianakon, O. Gruber, R. W. Harvey, C. C.  
474 Hegna, L. L. Lao, D. A. Monticello, F. Perkins, A. Pletzer, A. H. Reiman, M. Rosenbluth,  
475 E. J. Strait, T. S. Taylor, A. D. Turnbull, F. Waelbroeck, J. C. Wesley, H. R. Wilson, and  
476 R. Yoshino. Beta limits in long-pulse tokamak discharges. *Physics of Plasmas*, 4(5):1654–  
477 1664, 1997. doi:10.1063/1.872270. URL [http://link.aip.org/link/?PHP/4/  
478 1654/1](http://link.aip.org/link/?PHP/4/1654/1).
- 479 [32] A Schmid, A Herrmann, H W Müller, and the ASDEX Upgrade Team. Experimen-  
480 tal observation of the radial propagation of ELM induced filaments on ASDEX Upgrade.  
481 *Plasma Physics and Controlled Fusion*, 50(4):045007, 2008. URL [http://stacks.  
482 iop.org/0741-3335/50/i=4/a=045007](http://stacks.iop.org/0741-3335/50/i=4/a=045007).
- 483 [33] A Kirk, H W Muller, A Herrmann, M Kocan, V Rohde, P Tamain, and the ASDEX Up-  
484 grade Team. Parameters determining the radial propagation of type-I edge localized modes  
485 (ELMs) in ASDEX Upgrade. *Plasma Physics and Controlled Fusion*, 53(3):035003, 2011.  
486 URL <http://stacks.iop.org/0741-3335/53/i=3/a=035003>.